

CFI2P: Coarse-to-Fine Cross-Modal Correspondence Learning for Image-to-Point Cloud Registration

Gongxin Yao¹, Yixin Xuan², Yiwei Chen¹, Yu Pan^{1*}

¹Institute of Cyber-Systems and Control, Zhejiang University, Hangzhou 310027, China

²Polytechnic Institute, Zhejiang University, Hangzhou 310015, China

{yaogongxin, ypan}@zju.edu.cn

Abstract

In the context of image-to-point cloud registration, acquiring point-to-pixel correspondences presents a challenging task since the similarity between individual points and pixels is ambiguous due to the visual differences in data modalities. Nevertheless, the same object present in the two data formats can be readily identified from the local perspective of point sets and pixel patches. Motivated by this intuition, we propose a coarse-to-fine framework that emphasizes the establishment of correspondences between local point sets and pixel patches, followed by the refinement of results at both the point and pixel levels. On a coarse scale, we mimic the classic Visual Transformer to translate both image and point cloud into two sequences of local representations, namely point and pixel proxies, and employ attention to capture global and cross-modal contexts. To supervise the coarse matching, we propose a novel projected point proportion loss, which guides to match point sets with pixel patches where more points can be projected into. On a finer scale, point-to-pixel correspondences are then refined from a smaller search space (i.e., the coarsely matched sets and patches) via well-designed sampling, attentional learning and fine matching, where sampling masks are embedded in the last two steps to mitigate the negative effect of sampling. With the high-quality correspondences, the registration problem is then resolved by EPnP algorithm within RANSAC. Experimental results on large-scale outdoor benchmarks demonstrate our superiority over existing methods.

1 Introduction

Image-to-point cloud registration refers to the problem of estimating the camera pose (i.e., rotation and translation) of a query image with respect to the coordinate frame of a reference 3D map. It has wide applications in various computer vision tasks, including image-based localization (Chen, Xue, and Pang 2022; Lee et al. 2023) in visual Simultaneous Localization and Mapping (vSLAM) (Durrant-Whyte and Bailey 2006; Mur-Artal, Montiel, and Tardos 2015), visual pose estimation in Structure-from-Motion (SfM) (Ullman 1979; Cui et al. 2022), and camera extrinsic calibration for multi-sensor system with camera and LiDAR (Tsaregorodtsev et al. 2022; Liao et al. 2023). However, RGB images capture visual attributes like texture, color and luminosity through regular 2D grid structures,

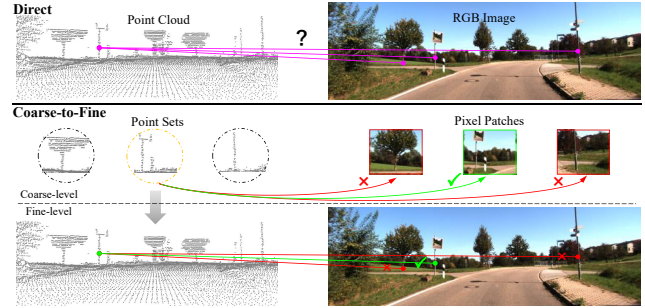


Figure 1: Comparison of the direct and coarse-to-fine mechanisms in building cross-modal correspondences from point clouds to images. The global ambiguity between similar points and pixels can be resolved with the high-level semantics represented by the local regions.

while unordered and irregular point clouds solely provide rich 3D geometric information. Such modality gaps pose a significant challenge for image-to-point cloud registration.

When the correspondences between 2D pixels and 3D points are available, the registration problem can be simplified to the traditional Perspective-n-Point (PnP) problem (Zheng et al. 2013). In this context, both the P3P (Gao et al. 2003) and EPnP (Lepetit, Moreno-Noguer, and Fua 2009) algorithms have proven to be effective in estimating the camera pose. However, establishing the point-to-pixel correspondences is non-trivial and coupled with pose estimation. In recent years, a prominent paradigm has emerged, with the primary objective of establishing correspondences in the feature space with deep learning. Subsequently, the aforementioned PnP solver is employed within RANSAC framework (Fischler and Bolles 1981) to solve the camera pose. 2D3D-MatchNet (Feng et al. 2019) adopted the hand-crafted SIFT (Lowe 1999) and ISS (Zhong 2009) operators to detect the interest pixels and points for matching. However, it suffers from low inlier ratio when establishing correspondences for these feature-independent pixels and points. DeepI2P (Li and Lee 2021) classified the 3D points projected in the camera frustum and utilized inverse camera projection to optimize the camera pose. This classification operation is equivalent to establishing a fuzzy correspondence and the registration accuracy is limited by the misclassified points around

*Corresponding author.

the frustum boundary. CorrI2P (Ren et al. 2022) adopted a metric learning framework (Ye et al. 2021) to learn discriminative descriptors for each pixel and point, while predicting a symmetric overlap region between the image and point cloud. However, establishing dense correspondences within such global overlap region still suffers from low inlier ratio and great complexity.

Coarse-to-fine mechanism has been leveraged by our same-modal counterparts, i.e., image-to-image registration (Zhou, Sattler, and Leal-Taixe 2021; Sun et al. 2021a; Mok and Chung 2022) and point-cloud registration (Yu et al. 2021a; Qin et al. 2022), which establish pixel-to-pixel and point-to-point correspondences. We argue that the coarse-to-fine mechanism will also play a role in establishing point-to-pixel correspondences for image-to-point cloud registration (as illustrated in Fig. 1). Nevertheless, designing a coarse-to-fine pipeline that incorporates and bridges the modality gaps between these two types of data, as well as addresses the unordered and irregular characteristics of point clouds, poses a non-trivial task.

In this paper, we propose a novel **Coarse-to-Fine Image-to-Point** cloud (CFI2P) registration framework, learning cross-modal correspondences in a progressive manner. Following the design philosophy of Transformer (Vaswani et al. 2017) in point clouds (Yu et al. 2021b) and images (Dosovitskiy et al. 2021), we abstract the point set in a local region gathered by grouping strategy (Li, Chen, and Lee 2018) as *Point Proxy* and the pixel patch in a local region is integrated as *Pixel Proxy*. Self and cross attention modules are then used alternately to capture global and cross-modal information between pixel and point proxies. To guide the learning of coarse matching, we propose a novel projected point proportion loss to measure the degree of correlation between point and pixel proxies. Highly correlated coarse matches are selected for further refinement, effectively narrowing down the search space of the subsequent operations. On a finer scale, to facilitate batch processing, we resample a fixed number of points and pixels according to the coarse matching proposals, and then repeat the similar learning and matching operations to establish point-to-pixel correspondences. To eliminate the negative effect of invalid sampled points and pixels, we propose a mask strategy to improve the local feature learning and fine correspondence extraction. Specifically, we design a masked-attention module to extract local interactive features between the points and pixels, and a projected point distance loss that is also embedded with masks to increase the fine matching accuracy. All the point-to-pixel correspondences with high confidence are collected to estimate the final camera pose. Comprehensive experiments on KITTI Odometry (Geiger et al. 2013) and NuScenes (Caesar et al. 2020) datasets demonstrate the superiority of the coarse-to-fine mechanism, improving the registration accuracy.

In conclusion, the main contributions of this paper are:

- A novel coarse-to-fine framework with a hybrid Transformer implementation to establish cross-modal correspondences for image-to-point cloud registration. It emphasizes to establish the correspondences between local point sets and pixel patches first.

- A novel projected point proportion loss to measure the degree of correlation between point proxy (i.e., point set) and pixel proxy (i.e., pixel patch) at a coarse level. The acquired coarse matches effectively squeeze the search space for the subsequent fine matching.
- A well-designed refining method to establish point-to-pixel correspondences, and a mask strategy is embedded in its components to mitigate the negative effect of invalid sampled points and pixels.

2 Related works

2.1 Image-to-Image Registration

Image-to-image registration (Ma et al. 2021) is a multi-view geometric problem, which aims to estimating the relative pose between two images taken from different locations. Due to the lack of depth information, epipolar constraint (Diel, DeBitetto, and Teller 2005; Zhou, Sattler, and Leal-Taixe 2021) is a classic method to describe the geometric relationship between the corresponding pixels in two different views of the same scene. Besides, many algorithms are usually based on pixel-to-pixel feature matching. For example, FFT(Reddy and Chatterji 1996), SFT (Lowe 1999) and ORB (Rublee et al. 2011) are the commonly used hand-crafted features to extract local geometric information. Superpoint (DeTone, Malisiewicz, and Rabinovich 2018), DualRC-Net (Li et al. 2020), SuperGlue (Sarlin et al. 2020), LoFTR (Sun et al. 2021b) and ACVNet (Xu et al. 2022) are the representative learning-based methods. However, these methods only work on the regular grid data.

2.2 Point Cloud Registration

Due to the inherent 3D geometric information, estimating the rigid transformation between two point clouds is relatively straightforward. ICP (Besl and McKay 1992) and its variants (Rusinkiewicz and Levoy 2001; Yang, Li, and Jia 2013) can directly iterative on the 3D points to optimize the transformation, but they are sensitive to initialization or have complexity scaling quadratically with the number of points. DCP (Wang and Solomon 2019) and PointNetLK (Aoki et al. 2019) are the seminal works that introduce deep learning to the task of point cloud registration. After that, the recent works (Huang et al. 2021; Lu et al. 2021; Yu et al. 2021a; Qin et al. 2022; Ao et al. 2023) attempted to take the architecture of KPConv (Thomas et al. 2019), which simulates grid convolution and pooling operations to extract local features and change the 3D point resolution. Although KPConv requires complex data preprocessing, it supports the above methods to establish accurate correspondences from coarse node to fine 3D point gradually. However, similar to image-to-image registration, the above methods don't work for cross-modal registration between image and point cloud.

2.3 Image-to-Point Cloud Registration

Considering the modality gaps between images and point clouds, 2D3D-MatchNet (Feng et al. 2019) detects sparse key pixels and points by SIFT (Lowe 1999) and ISS (Zhong 2009) first. Following this, the surrounding patches of these

key pixels and points are fed into a pseudo-siamese neural network (Hoffer and Ailon 2015; Xu et al. 2019) to learn discriminative descriptors and establish 2D-3D correspondences. Camera pose estimation is then performed using a RANSAC-based EPnP (Lepetit, Moreno-Noguer, and Fua 2009) solver. However, because of the different feature extraction modes of ISS and SIFT operators, there is no guarantee that the extracted SIFT pixels and ISS points are correlated. Hence, 2D3D-MatchNet is prone to having a low inlier ratio. DeeI2P (Li and Lee 2021) is a detection-free method that interprets the registration problem as a classification problem, whereby the point cloud projected in the camera frustum is classified and then utilize inverse camera projection to estimate camera pose. This classification operation is equivalent to establishing a fuzzy correspondence between point cloud and image. The final registration accuracy is limited by the misclassified points around the frustum boundary, and the inverse camera projection also requires good pose initialization. CorrI2P (Ren et al. 2022) follows the same metric learning paradigm as 2D3D-MatchNet to learn discriminative descriptors for all pixels and points, while simultaneously predicting a symmetric overlap region between image and point cloud. To establish point-to-pixel correspondences, each point should search for its nearest 2D pixel in the feature space and the overlap region. As a result, the large search space makes this method prone to many false matches and has significant complexity.

3 Methodology

3.1 Overview

Given a query RGB image $\mathbf{I} \in \mathbb{R}^{H \times W \times 3}$ with a resolution of $H \times W$, and a reference point cloud $\mathbf{P} \in \mathbb{R}^{N \times 3}$ with N points $\mathbf{p}_i \in \mathbb{R}^3$, our goal is to estimate a rigid transformation $\bar{\mathbf{T}} = [\bar{\mathbf{R}} \mid \bar{\mathbf{t}}]$ (i.e., the camera pose) with a rotation $\bar{\mathbf{R}} \in SO(3)$ and a translation $\bar{\mathbf{t}} \in \mathbb{R}^3$, which aligns the coordinate frames of the camera and point cloud. It is equivalent to minimizing the following square error:

$$\bar{\mathbf{T}} = \arg \min_{\mathbf{T}} \sum_{(\mathbf{u}_i, \mathbf{p}_i) \in C^*} \|\mathbf{u}_i - \mathcal{F}_p(\mathbf{K}\mathbf{T}\mathbf{p}_i)\|^2, \quad (1)$$

where $\|\cdot\|$ represents the Euclidean distance, C^* is the set of ground-truth point-to-pixel correspondences, $\mathbf{u}_i = [u_i, v_i]^\top$ is a 2D pixel coordinates, $\mathbf{K} \in \mathbb{R}^{3 \times 3}$ is the camera intrinsic matrix, $\mathbf{T}\mathbf{p}_i$ implicitly converts \mathbf{p}_i from inhomogeneous to homogeneous coordinates (i.e., $\mathbf{p}_i \rightarrow [\mathbf{p}_i, 1]^\top$) and then performs matrix product. $\mathcal{F}_p(\cdot)$ is a planar projection function:

$$\mathcal{F}_p([x, y, z]^\top) = [u', v']^\top = [x/z, y/z]^\top. \quad (2)$$

We follow the paradigm of establishing point-to-pixel correspondences first and then estimating the relative pose with RANSAC-based EPnP solver (Lepetit, Moreno-Noguer, and Fua 2009), where our primary focus is on the former. We argue that pixel patch and local point set are more conducive to extracting semantically consistent features, which in turn enable set-to-patch correspondences to be established. Thus, the point-to-pixel correspondences are restricted to a smaller space. As illustrated in Fig. 2, our proposed CFI2P is a coarse-to-fine framework that follows the above viewpoint.

We will introduce our method and the novel coarse-to-fine supervision in detail as follows.

3.2 Proxy Generation

To make the 2D images \mathbf{I} and the 3D point clouds \mathbf{P} suitable for coarse-to-fine mechanism, the first step is to extract the coarse representations, namely *pixel proxy* and *point proxy*.

For 2D images, we use a standard ResNet (He et al. 2016) architecture to extract feature $\mathbf{F}'_{\mathbf{I}} \in \mathbb{R}^{H' \times W' \times d_f}$. Since 2D images have a compact and regular grid data structure, we follow the Vision Transformer (Dosovitskiy et al. 2021) to split \mathbf{I} into non-overlapping patches $\{\mathbf{I}_1, \mathbf{I}_2, \dots, \mathbf{I}_{N_I}\}$ with a resolution of $w \times w$, and then use a linear projection layer to project their features as the pixel proxies with arbitrary feature dimension $\mathbf{F}'_{\mathbf{I}} \in \mathbb{R}^{N_I \times d_p}$, where $N_I = H'W'/w^2$.

Since 3D point clouds are unordered and irregular, a standard PointNet (Qi et al. 2017a) architecture is adopted to extract point-wise features $\mathbf{F}'_{\mathbf{P}} \in \mathbb{R}^{N \times d_f}$. Simultaneously, we conduct Farthest Point Sampling (FPS) to obtain a fixed number of points $\mathbf{Q} = \{\mathbf{q}_1, \mathbf{q}_2, \dots, \mathbf{q}_{N_q}\}$, which will serve as the centers of some local regions. The associated features are denoted as $\mathbf{F}'_{\mathbf{Q}} \in \mathbb{R}^{N_q \times d_f}$. Then, we take a point-to-node grouping (Li, Chen, and Lee 2018) strategy to assign every point in \mathbf{P} to its nearest center in \mathbf{Q} . After grouping, the raw point cloud \mathbf{P} is splitted into N_q point sets $G^{\mathbf{P}} = \{G_1^{\mathbf{P}}, G_2^{\mathbf{P}}, \dots, G_{N_q}^{\mathbf{P}}\}$ as well as their associated feature sets $G^{\mathbf{F}'} = \{G_1^{\mathbf{F}'}, G_2^{\mathbf{F}'}, \dots, G_{N_q}^{\mathbf{F}'}\}$:

$$\begin{cases} G_j^{\mathbf{P}} = \{\mathbf{p}_i \in \mathbf{P} \mid \|\mathbf{p}_i - \mathbf{q}_j\| \leq \|\mathbf{p}_i - \mathbf{q}_k\|, k \neq j\} \\ G_j^{\mathbf{F}'} = \{\mathbf{F}'_{\mathbf{p}_i} \in \mathbf{F}'_{\mathbf{P}} \mid \mathbf{p}_i \in G_j^{\mathbf{P}}\} \end{cases}. \quad (3)$$

Here, the normal linear projection layer can not handle $G_j^{\mathbf{P}}$ as the quantity of points present in different $G_j^{\mathbf{P}}$ varies. We modified a standard Point Transformer (Zhao et al. 2021) layer with *torch_scatter*¹ indexing (namely Attentive Aggregation. See Appendices Section A.1) to aggregate uniform features for these heterogeneous $G^{\mathbf{P}}$ and $G^{\mathbf{F}'}$. For this purpose, \mathbf{q}_j and its features $\mathbf{F}'_{\mathbf{q}_j}$ are taken as the *Query* vectors, while the grouped points $G_j^{\mathbf{P}}$ and features $G_j^{\mathbf{F}'}$ are the *Key* and *Value* vectors. We get the point proxies $\mathbf{F}'_{\mathbf{q}_j} \in \mathbb{R}^{N_q \times d_p}$ where a single proxy $\mathbf{F}'_{\mathbf{q}_j} \in \mathbb{R}^{d_p}$ is computed with vector attention (Zhao et al. 2021) as:

$$\mathbf{F}'_{\mathbf{q}_j} = \sum_{\mathbf{p}_i \in G_j^{\mathbf{P}}} \rho(\gamma(\varphi(\mathbf{F}'_{\mathbf{q}_j}) - \psi(\mathbf{F}'_{\mathbf{p}_i}) + \delta)) \odot (\alpha(\mathbf{F}'_{\mathbf{p}_i}) + \delta), \quad (4)$$

where $\delta = \theta(\mathbf{q}_j - \mathbf{p}_i)$ is the point positional embedding and θ projects relative position to the feature space. γ, φ, ψ and α are point-wise MLPs or linear projections that changes the feature dimension. ρ is a normalization function such as *softmax* and it computes an attention weight vector for every feature channels. \odot represents Hadamard product.

3.3 Proxy Learning

So far, the proxies $\mathbf{F}'_{\mathbf{I}}$ and $\mathbf{F}'_{\mathbf{Q}}$ only encode their local geometry, but they both lack global and cross-modal contexts.

¹A public library for complex indexing.

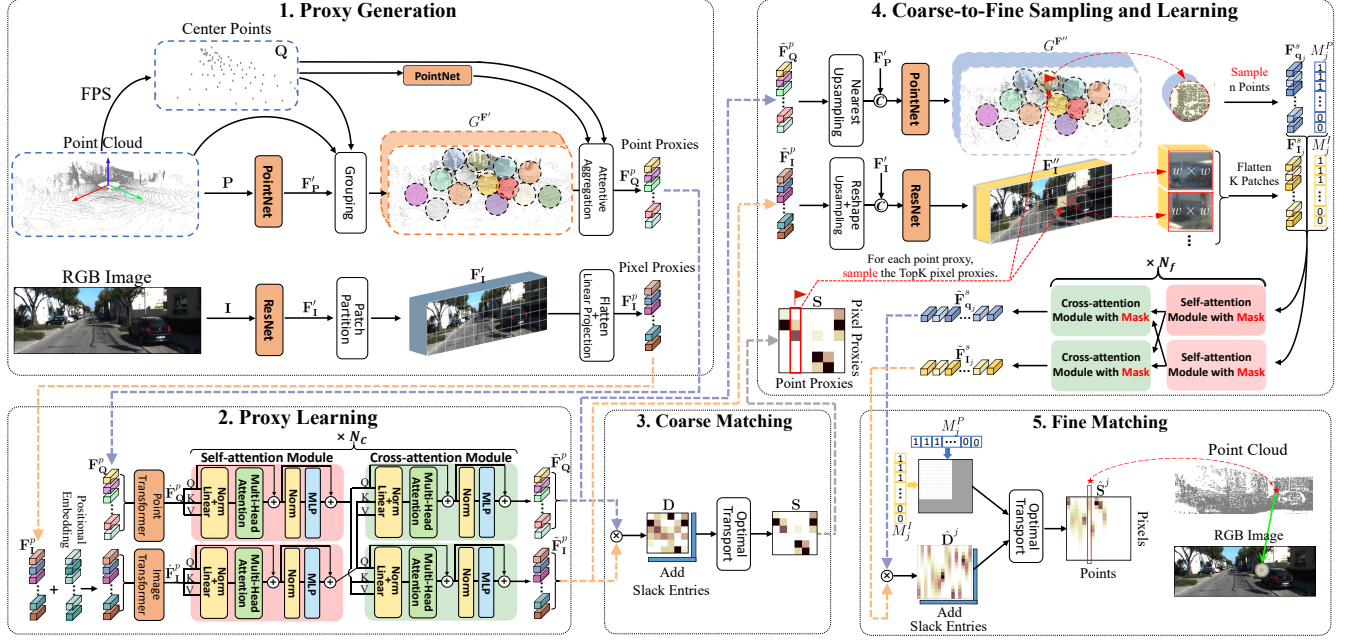


Figure 2: **Overview of the proposed CFI2P Framework.** 1). We first convert the image and the point cloud to two sets of feature vectors, namely *pixel* and *point proxies*, that represent the local geometry. 2). By analogy to the classic information interaction pipeline, the proxy learning module treats the proxies as 1D sequences and updates them with self-attention and cross-attention. 3). The coarse matching module establishes the coarse correspondences between the point proxies and pixel proxies. 4). The next coarse-to-fine module resamples and learns the point-level and pixel-level features according to the coarse correspondences. 5). The final point-to-pixel correspondences are established and collected with the fine matching module.

Following the standard Vision Transformer, we treat \mathbf{F}_I^P as a 1D sequence and add sinusoidal position embeddings to retain the positional information. Then, a transformer encoder is utilized to enhance \mathbf{F}_I^P with both long-range and short-range information. A single update step in the transformer is implemented with standard scalar dot-product attention as:

$$\mathbf{F}_I^P = \mathbf{F}_I^P + \text{softmax}\left(\frac{\mathbf{F}_I^P \mathbf{W}_Q (\mathbf{F}_I^P \mathbf{W}_K)^T}{\sqrt{d_p}}\right) (\mathbf{F}_I^P \mathbf{W}_V), \quad (5)$$

where $\mathbf{W}_Q/\mathbf{W}_K/\mathbf{W}_V \in \mathbb{R}^{d_p \times d_p}$ are the learnable parameters of the corresponding (i.e., *Query*, *Key*, and *Value*) linear projection layers. For each feature vector, a scalar attention weight is computed for all channels.

To capture global contexts for the point proxies \mathbf{F}_Q^P , we utilize the standard Point Transformer that increases the receptive field gradually. For a single Point Transformer layer, we will perform a vector attention operation to learn the residual term of $\mathbf{F}_{q_j}^P$ as:

$$\mathfrak{R} = \sum_{\mathbf{q}_i \in \mathcal{X}(\mathbf{q}_j)} \rho(\gamma(\varphi(\mathbf{F}_{q_j}^P) - \psi(\mathbf{F}_{q_i}^P) + \delta)) \odot (\alpha(\mathbf{F}_{q_i}^P) + \delta), \quad (6)$$

where $\mathcal{X}(\mathbf{q}_j)$ represents the k nearest neighbor center points of \mathbf{q}_j , and other calculation symbols follow the same definition in Eq. 4. Then we update $\dot{\mathbf{F}}_{q_j}^P = \mathbf{F}_{q_j}^P + \mathfrak{R}$. After several iterations, $\dot{\mathbf{F}}_{q_j}^P$ will be global-aware.

To exchange information between the enhanced \mathbf{F}_I^P and \mathbf{F}_Q^P , we uniformly adopt the scalar dot-product attention

mechanism in Eq. 5 to alternately implement self-attention and cross-attention. The acquired proxies with hybrid information are denoted as $\tilde{\mathbf{F}}_Q^P \in \mathbb{R}^{N_q \times d_p}$ and $\tilde{\mathbf{F}}_I^P \in \mathbb{R}^{N_I \times d_p}$.

3.4 Coarse Matching

By matching the pixel and point proxies, this module provides a preliminary localization for the subsequent fine-level operations. Note that in 2D and 3D geometric space, these proxies represent pixel patches and point sets, respectively. Therefore, our objective is equivalent to associating each point set with the pixel patches, where the 3D points are projected in the corresponding field-of-views (FoVs). To this end, we first compute a pairwise distance matrix $\mathbf{D} \in \mathbb{R}^{N_I \times N_q}$ as:

$$\mathbf{D} = \tilde{\mathbf{F}}_I^P (\tilde{\mathbf{F}}_Q^P)^T / \sqrt{d_p}, \quad (7)$$

where each entry \mathbf{D}_{ij} measures the cost of assigning a pixel proxy $\tilde{\mathbf{F}}_I^P$ to a point proxy $\tilde{\mathbf{F}}_Q^P$. Since not all point proxies will have at least one pixel proxy associated with them and vice versa, we append a row and a column of learnable parameters to \mathbf{D} as the slack entries, which enables some proxies to be assigned to. Based on it, we then utilize a differentiable optimal transport algorithm (Sarlin et al. 2020) to seek an optimal matching score matrix $\mathbf{S} \in \mathbb{R}^{N_I \times N_q}$, where the slack entries are removed after convergence. A higher score \mathbf{S}_{ij} represents that more points of $\tilde{\mathbf{F}}_Q^P$ can be projected into the FoV of $\tilde{\mathbf{F}}_I^P$.

3.5 Coarse-to-Fine Sampling and Learning

To fuse both global and cross-modal information to a finer resolution, we concatenate the reshaped and upsampled $\tilde{\mathbf{F}}_{\mathbf{I}}^p$ with $\mathbf{F}'_{\mathbf{I}}$, and feed them into a ResNet to learn pixel-wise features $\mathbf{F}''_{\mathbf{I}} \in \mathbb{R}^{H' \times W' \times d_f}$. Similarly, each point proxy $\tilde{\mathbf{F}}_{\mathbf{q}_j}^p$ is replicated $|G_j^p|$ times, where $|\cdot|$ denotes the set cardinality, concatenated with G_j^p , and fed into a PointNet to learn point-wise features $G_j^{p''} \in \mathbb{R}^{|G_j^p| \times d_f}$. The associated feature sets are $G'' = \{G_1^{p''}, \dots, G_{N_q}^{p''}\}$.

According to the coarse matching score matrix \mathbf{S} , we only establish finer point-to-pixel correspondences for the j -th point proxy that satisfies $\sum_{i=1}^{N_I} \mathbf{S}_{ij} > 0$. To facilitate batch processing, we first sample n points in each point proxy (i.e., point set G_j^p) and the associated features are denoted as $\mathbf{F}_{\mathbf{q}_j}^s \in \mathbb{R}^{n \times d_f}$. Another byproduct of this sampling is a binary point mask $M_j^P \in \mathbb{R}^{n \times 1}$, where the first $|G_j^p|$ items are 1 and the last $(n - |G_j^p|)$ items are 0 if $|G_j^p| < n$. On the other hand, we also sample the pixel proxies (i.e., pixel patches with a resolution of $w \times w$) of the top k items in the j -th column of \mathbf{S} . The associated features are $\mathbf{F}_{\mathbf{I}_j}^s \in \mathbb{R}^{m \times d_f}$ where $m = k \times w \times w$, and the similar binary pixel mask is $M_j^I \in \mathbb{R}^{m \times 1}$ where the first $k' \times w \times w$ items are 1 and the last $(k - k') \times w \times w$ items are 0 if there are k' items > 0 in the j -th column of \mathbf{S} and $k' < k$.

Afterwards, we will extract the interactive features between $\mathbf{F}_{\mathbf{q}_j}^s$ and $\mathbf{F}_{\mathbf{I}_j}^s$. To eliminate the negative effect of invalid sampled points and pixels, we embed the above masks into the attention mechanism for focusing. Take cross-attention module with mask as an example, we replicate M_j^P and M_j^I as $\mathbf{M}_j^P \in \mathbb{R}^{n \times d_f}$ and $\mathbf{M}_j^I \in \mathbb{R}^{m \times d_f}$. The attention weight $\mathbf{W}_a \in \mathbb{R}^{m \times n}$ between $\mathbf{F}_{\mathbf{q}_j}^s$ and $\mathbf{F}_{\mathbf{I}_j}^s$ is calculated as:

$$\mathbf{W}_a = \text{softmax}\left(\frac{\left(\mathbf{M}_j^I \odot (\mathbf{F}_{\mathbf{I}_j}^s \mathbf{W}_Q)\right) \left(\mathbf{M}_j^P \odot (\mathbf{F}_{\mathbf{q}_j}^s \mathbf{W}_K)\right)^T}{\sqrt{d_f}}\right), \quad (8)$$

and we fuse the information from $\mathbf{F}_{\mathbf{q}_j}^s$ to $\mathbf{F}_{\mathbf{I}_j}^s$ as:

$$\mathbf{F}_{\mathbf{I}_j}^s = \mathbf{F}_{\mathbf{I}_j}^s + \mathbf{W}_a \left(\mathbf{M}_j^P \odot (\mathbf{F}_{\mathbf{q}_j}^s \mathbf{W}_V)\right), \quad (9)$$

where $\mathbf{W}_Q / \mathbf{W}_K / \mathbf{W}_V \in \mathbb{R}^{d_f \times d_f}$ are the learnable parameters, and \odot represents Hadamard product. The acquired point-wise and pixel-wise features with hybrid information are denoted as $\tilde{\mathbf{F}}_{\mathbf{q}_j}^s \in \mathbb{R}^{n \times d_f}$ and $\tilde{\mathbf{F}}_{\mathbf{I}_j}^s \in \mathbb{R}^{m \times d_f}$.

3.6 Fine Matching

In this module, we still utilize the differentiable optimal transport algorithm to establish point-to-pixel correspondences. Especially, we incorporate the point mask M_j^P and the pixel mask M_j^I into the calculation of the pairwise distance matrix $\hat{\mathbf{D}}^j \in \mathbb{R}^{m \times n}$ as:

$$\hat{\mathbf{D}}^j = \left(M_j^I (M_j^P)^T\right) \odot \left(\tilde{\mathbf{F}}_{\mathbf{I}_j}^s (\tilde{\mathbf{F}}_{\mathbf{q}_j}^s)^T\right) / \sqrt{d_f}. \quad (10)$$

Since not all sampled points can be projected into the sampled pixel patches and the sampled pixels are generally redundant, a row and a column of learnable parameters are

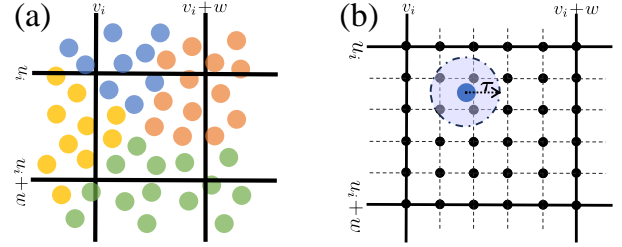


Figure 3: Illustration of the projected points. (a) At a coarse level, the points from different sets (colors represent sets) are projected into the same pixel patch. (b) At a fine level, the pixels (black spots) with a distance of less than τ from the projected point (blue spot) are positive.

also appended to $\hat{\mathbf{D}}^j$ as the slack entries. After convergence, we remove the slack entries and get a point-to-pixel matching score matrix $\hat{\mathbf{S}}^j \in \mathbb{R}^{m \times n}$, where each column is normalized to a 1D probability distribution. By computing expectation or selecting the maximum over each column, we get a correspondence from a point to a pixel.

We repeat the fine matching operation on the resampled points and pixels of all coarsely matched point proxies. All point-to-pixel correspondences are collected for the final image-to-point cloud registration.

3.7 Supervision

The coarse and fine parts of CFI2P are trained separately.

Coarse-level Supervision. We propose a novel projected point proportion loss to supervise the coarse score matrix S . Obviously, the 3D points belonging to different sets can be projected into the same pixel patch as illustrated in Fig. 3 (a). Denote the X-axis and Y-axis range of the pixel patch \mathbf{I}_i as $\Gamma_i^x = (u_i, u_i + w)$ and $\Gamma_i^y = (v_i, v_i + w)$, we compute the ratio of points in set G_j^p that can be projected into \mathbf{I}_i as:

$$r_{ij}^{\leftarrow} = \frac{\left|\{\tilde{\mathbf{p}} \in G_j^p \mid [\tilde{u}, \tilde{v}]^T = \mathcal{F}_p(\mathbf{K}\bar{\mathbf{T}}\tilde{\mathbf{p}}), \tilde{u} \in \Gamma_i^x, \tilde{v} \in \Gamma_i^y\}\right|}{|G_j^p|}. \quad (11)$$

On the contrary, we compute the ratio of points in \mathbf{I}_i that are projected from point set G_j^p as:

$$r_{ij}^{\rightarrow} = \frac{\left|\{\tilde{\mathbf{p}} \in G_j^p \mid [\tilde{u}, \tilde{v}]^T = \mathcal{F}_p(\mathbf{K}\bar{\mathbf{T}}\tilde{\mathbf{p}}), \tilde{u} \in \Gamma_i^x, \tilde{v} \in \Gamma_i^y\}\right|}{\left|\{\tilde{\mathbf{p}} \in \mathbf{P} \mid [\tilde{u}, \tilde{v}]^T = \mathcal{F}_p(\mathbf{K}\bar{\mathbf{T}}\tilde{\mathbf{p}}), \tilde{u} \in \Gamma_i^x, \tilde{v} \in \Gamma_i^y\}\right|}. \quad (12)$$

Based on the above r_{ij}^{\leftarrow} and r_{ij}^{\rightarrow} with different orientations, we define a weight matrix $\mathbf{W}^c \in \mathbb{R}^{(N_I+1) \times (N_q+1)}$ as:

$$\mathbf{W}_{ij}^c = \begin{cases} \min(r_{ij}^{\leftarrow}, r_{ij}^{\rightarrow}), & i \leq N_I \wedge j \leq N_q, \\ 1 - \sum_k r_{ik}^{\rightarrow}, & i \leq N_I \wedge j = N_q + 1, \\ 1 - \sum_k r_{kj}^{\leftarrow}, & i = N_I + 1 \wedge j \leq N_q, \\ 0, & \text{otherwise.} \end{cases} \quad (13)$$

The final loss is defined as a weighted negative log-likelihood loss (Sarlin et al. 2020; Yu et al. 2021a) as:

$$\mathcal{L}_c = \frac{-\sum_{i,j} \mathbf{W}_{ij}^c \log(\mathbf{S}_{ij})}{\sum_{i,j} \mathbf{W}_{ij}^c}. \quad (14)$$

Fine-level Supervision. We design a projected point distance loss with mask to supervise the fine score matrix $\hat{\mathbf{S}}^\ell$ of the ℓ -th coarsely matched point proxy. Denote the resampled 3D points as $\{\mathbf{p}_1^\ell, \dots, \mathbf{p}_n^\ell\}$, the point mask as $M_\ell^P \in \mathbb{R}^{n \times 1}$, the 2D coordinates of the resampled pixels as $\{\mathbf{u}_1^\ell, \dots, \mathbf{u}_m^\ell\}$, and the pixel mask as $M_\ell^I \in \mathbb{R}^{m \times 1}$. We define a binary matrix $\mathbf{W}^\ell \in \mathbb{R}^{(m+1) \times (n+1)}$ where any \mathbf{W}_{ij}^ℓ subject to $i \leq m$ and $j \leq n$ is computed as:

$$\mathbf{W}_{ij}^\ell = \begin{cases} 1, & \|\mathbf{u}_i^\ell - \mathcal{F}_p(\mathbf{K}\bar{\mathbf{T}}\mathbf{p}_j^\ell)\| \leq \tau, \\ 0, & \|\mathbf{u}_i^\ell - \mathcal{F}_p(\mathbf{K}\bar{\mathbf{T}}\mathbf{p}_j^\ell)\| > \tau, \end{cases} \quad (15)$$

where τ is a distance threshold to classify the positive pixel with respect to a projected point as shown in Fig. 3 (b). Synchronized with Eq. 10, we then mask the above $m \times n$ elements in \mathbf{W}^ℓ with $M_\ell^I(M_\ell^P)^\top$. Other elements on the edges in \mathbf{W}^ℓ are then computed as:

$$\mathbf{W}_{ij}^\ell = \begin{cases} \max(0, 1 - \sum_{i'=1}^m \mathbf{W}_{i'j}^\ell), & i = m+1 \wedge j \leq n, \\ \max(0, 1 - \sum_{j'=1}^n \mathbf{W}_{ij'}^\ell), & i \leq m \wedge j = n+1, \\ 0, & i = m+1 \wedge j = n+1. \end{cases} \quad (16)$$

The final loss is the sum of the weighted negative log-likelihood loss across all coarsely matched point proxies:

$$\mathcal{L}_f = \sum_\ell \frac{-\sum_{i,j} \mathbf{W}_{ij}^\ell \log(\hat{\mathbf{S}}_{ij}^\ell)}{\sum_{i,j} \mathbf{W}_{ij}^\ell}. \quad (17)$$

4 Experiments

4.1 Experimental Setup

Dataset. We conducted experiments on two large-scale outdoor benchmarks, i.e., KITTI Odometry (Geiger et al. 2013) and NuScenes (Caesar et al. 2020) datasets. For a fair comparison, we follow the same operations in the previous works (Li and Lee 2021; Ren et al. 2022) to get image-point cloud pairs. The detailed description can be found in Appendices Section A.2.

Implementation Details. In the proxy generation, an image is splitted into patches with a resolution of 8×8 while a point cloud is splitted into 256 sets. So the number of pixel and point proxies are $(H' \times W')/64$ and 256. In the coarse-to-fine sampling, we randomly sample $n=65$ points in each point set \hat{G}_j^P and select the top 3 pixel proxies (i.e., $m=3 \times 64$) according to the coarse matching scores. The distance threshold τ in Eq. 15 is 1 pixel. We collect the point-to-pixel correspondences output by CFI2P and then used a RANSAC-based EPnP solver to estimate the transformation. The number of RANSAC iterations is 500 and the threshold for inlier reprojection error is 1. We trained our CFI2P on an NVIDIA RTX 3090 GPU with an ADAM optimizer. Please refer to Appendices Section A.2 for more training details.

Evaluation Metrics. Similar to point cloud registration (Qin et al. 2022), we evaluate the accuracy of point-to-pixel correspondences with four metrics: 1-2). *Inlier Ratio* before (IR) and after (IRR) RANSAC iteration. It is the fraction of inliers among all putative correspondences. A correspondence is considered as an inlier if the distance between the

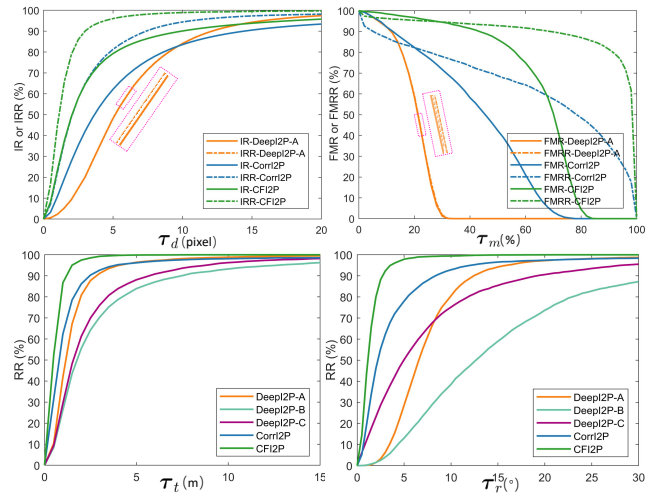


Figure 4: Curves of the evaluation metrics with various thresholds. We obtained them on KITTI Odometry dataset.

projected point and the ground-truth pixel is smaller than a threshold τ_d . 3-4). *Feature Matching Recall* before (FMR) and after (FMRR) RANSAC iteration. It is the fraction of data pairs whose inlier ratio is above a threshold τ_m . Besides, following DeepI2P (Li and Lee 2021), we also evaluate the registration performance with three metrics: 1). The mean of relative rotation error (RRE). 2). The mean of relative translation error (RTE). 3). *Registration Recall* (RR), the fraction of successful registrations among the test dataset. A registration is considered as successful when the RRE is smaller than τ_r and the RTE is smaller than τ_t . See Appendices Section B for detailed definitions.

Baseline Algorithms. We compare our CFI2P with four state-of-the-art algorithms: 1-3). The three variants described in DeepI2P (Li and Lee 2021), including DeepI2P-A that divides the image into 32×32 patches and classifies which patch the points of the point cloud are projected into, DeepI2P-B that uses the frustum classification and 3D inverse camera projection, and DeepI2P-C that uses the frustum classification and 2D inverse camera projection. 4). The recent overlap-based method CorrI2P (Ren et al. 2022) with a metric-learning architecture. Note that DeepI2P-B and DeepI2P-C do not establish point-to-pixel correspondences.

4.2 Evaluation

Correspondence results. To evaluate the correspondence accuracy, we first report the quantitative results in Tab. 1, where the threshold τ_d is set to 1 pixel (for IR and IRR) and τ_m is set to 10% (for FMR and FMRR). Our method has significant advantages in all the above metrics, especially in term of IR, CFI2P outperforms the second best method by over 20% on both KITTI Odometry and NuScenes. To investigate the robustness of the above advantages, the curves of the metrics with various thresholds are given in Fig. 4 (top two). Besides, we also visualize an example of the point-to-pixel correspondences in Fig. 5 (a).

	KITTI Odometry Dataset							NuScenes Dataset							Params(MB)
	IR(%)	IRR(%)	FMR(%)	FMRR(%)	RR(%)	RTE(m)	RRE(°)	IR(%)	IRR(%)	FMR(%)	FMRR(%)	RR(%)	RTE(m)	RRE(°)	
DeepI2P-A	20.21	20.30	92.12	92.28	80.18	1.13	5.88	24.99	35.52	95.62	94.93	62.67	2.22	7.37	105.6
DeepI2P-B	NA	NA	NA	NA	38.34	1.21	6.08	NA	NA	NA	NA	18.82	1.73	7.06	105.6
DeepI2P-C	NA	NA	NA	NA	74.50	1.42	3.87	NA	NA	NA	NA	92.53	1.95	3.02	105.6
CorrI2P	42.18	64.98	92.21	87.03	92.19	0.90	2.72	51.99	74.32	97.34	92.96	93.87	1.70	2.32	148.3
CFI2P	64.67	90.11	98.48	96.29	99.37	0.59	1.39	66.94	90.53	98.48	96.73	99.01	1.12	1.46	34.7

Table 1: Quantitative results of point-to-pixel correspondences and image-to-point cloud registration on the KITTI Odometry and NuScenes datasets. DeepI2P-B and DeepI2P-C are not correspondence-based methods.

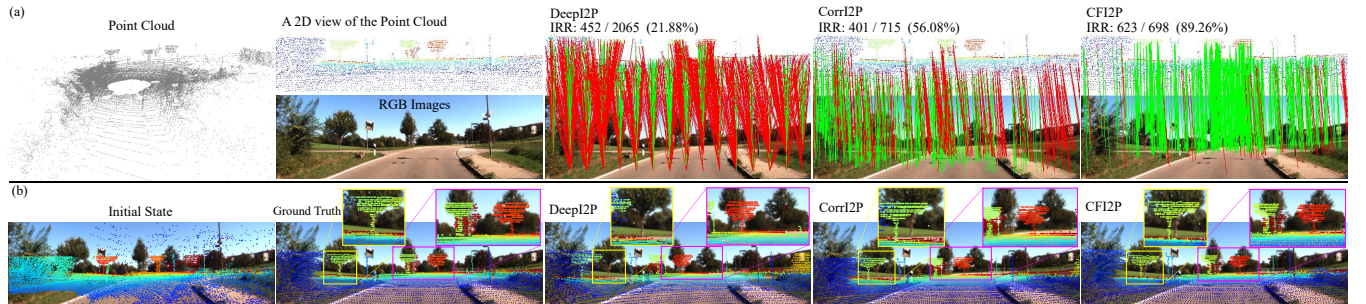


Figure 5: Qualitative results on the KITTI Odometry dataset. (a) To visualize the correct (green) and incorrect (red) point-to-pixel correspondences, the point cloud (gray) is projected into a narrow 2D view (point color indicates distance). For DeepI2P, the correspondences are obtained with DeepI2P-A. (b) Image-to-point cloud registration is equivalent to aligning the corresponding pixels and points. For DeepI2P, we show the best registration results obtained with DeepI2P-C.

Registration results. As illustrated in Tab. 1, our method is optimal on the three metrics due to better point-to-pixel correspondences, and the registration recall is even above 99% on both two datasets. Here, the RRE threshold τ_r is set to 10° and the RTE threshold τ_t is set to 5 m. We also show the registration recall curves with various RTE and RRE thresholds in Fig. 4 (bottom two). Note that we achieve this superior performance with only about a quarter of the parameters of CorrI2P. A registration example is visualized in Fig. 5 (b). Given a point cloud and image pair, the initial state of the projected points is chaotic due to the unknown camera pose. It is clear that our CFI2P has the best visual performance for point-pixel alignment since the estimated camera pose is closest to the ground truth.

Please refer to Appendices Section C for more results.

4.3 Ablation Study

We conducted ablation studies on the KITTI Odometry dataset to further analyze the effect of different components, including the attentive aggregation (AA), the attention modules (ATT) to capture cross-modal information, the coarse-to-fine mechanism (C2F), and the mask strategy (Mask) in the fine-level attention and matching operations. Without AA, we replace it with max pooling to generate point proxies. Without C2F, we replace the coarse-to-fine operations with the overlap detection and metric learning head in CorrI2P, and then search the nearest pixels from the overlap region. As illustrated in Tab. 2, all components contribute to the performance of the model, while C2F and Mask are the most noticeable. The results demonstrate the superiority of the coarse-to-fine mechanism, and the priori information

AA	ATT	C2F	Mask	IR(%)	RTE(m)	RRE(°)
	✓	✓	✓	53.50	0.922	1.839
✓		✓	✓	55.49	0.756	1.770
✓	✓		✓	50.83	0.907	2.252
✓	✓	✓		35.68	1.254	2.275
✓	✓	✓	✓	64.67	0.594	1.395

Table 2: Ablation studies of the components in CFI2P.

of the coarse-to-fine sampling carried by the mask is highly valuable. Furthermore, we have also investigated the effect of point cloud density and coarse-to-fine sampling density. Please see Appendices Section D.

5 Conclusion

This paper presents a novel coarse-to-fine framework for image-to-point cloud registration, named CFI2P, that can establish cross-modal correspondences between point clouds and RGB images. The proposed CFI2P follows the design philosophy of Transformers to abstract the local point sets and pixel patches as local proxies while adopting self and cross attention to transform the proxies to be global-aware and cross modal-aware. To match the cross-modal proxies, CFI2P is trained with the novel projected point proportion loss that can measure the degree of correlation between the point sets and pixel patches. After that, we refine these set-to-patch correspondences to pixel and point level with our specially designed coarse-to-fine resampling, learning and matching. Extensive experiments on large-scale outdoor scenes demonstrate the effectiveness of our method.

Appendices

A More Implementation Details

A.1 Attentive Aggregation

The Attentive Aggregation module adopts `torch_scatter` to index the points in different sets. Here, we provide an example with 4 point sets and show its detailed computation graph in Fig. 6. Given the center point set $\mathbf{Q} = \{\mathbf{q}_1, \mathbf{q}_2, \mathbf{q}_3, \mathbf{q}_4\}$, we use four colors (i.e., blue, orange, brown, pink) to index the point sets $G^P = \{G_1^P, G_2^P, G_3^P, G_4^P\}$ grouped by the center points. \mathbf{P} is the raw point cloud, \mathbf{F}'_Q is the associated features of \mathbf{Q} and \mathbf{F}'_P is the associated features of \mathbf{P} . To generate point proxies, \mathbf{F}'_Q is fed into a MLP φ and the output will act as *Query*, while \mathbf{F}'_P is fed into a MLP ψ and the output will act as *Key*. Since *Query* and *Key* have different point quantities and conform to surjection from *Key* to *Query*. We duplicate *Query* at the corresponding position according to the indices, then subtract *Key* and add the point positional embedding δ . The above result is processed by another MLP γ . The point positional embedding δ is obtained through a similar duplicate-sum operation and a MLP θ , except that the raw input is the 3D coordinates. After that, a separate softmax function will be performed inside each point set to get the attention weight. Note that each point set needs to subtract its maximum value to prevent numerical overflow in exponential calculations. \mathbf{F}'_P is also fed into a MLP α and the output will act as *Value*. The output *value* will add the point positional embedding δ , multiply by the above attention weights and finally sum inside each point set to obtain point proxies \mathbf{F}'_Q^P .

A.2 Dataset and Training Details

We use two outdoor LiDAR-Camera datasets in this paper.

KITTI Odometry There are 11 sequences that include the calibration parameters in this dataset. The data sequences 0-8 are used for training while 9-10 for testing. For a point cloud and image pair, we sample 40960 points per point cloud and resize the image as 160×512 . We first trained the coarse part of CFI2P for 60 epochs, with a batch size of 8. The initial learning rate is $1e-3$ and multiplied by 0.8 every 6 epochs. After convergence, we then fine-tuned the fine part of CFI2P for 5 epochs, with a batch size of 3. The initial learning rate is $5e-4$ and multiplied by 0.6 every epoch.

NuScenes This dataset includes 1000 scenes. We use the official SDK to split 850 scenes for training and 150 for testing. For a point cloud and image pair, we sample 40960 points per point cloud and resize the image as 160×320 . We first trained the coarse part of CFI2P for 30 epochs, with a batch size of 8. The initial learning rate is $1e-3$ and multiplied by 0.8 every 3 epochs. After convergence, we then fine-tuned the fine part of CFI2P for 3 epochs, with a batch size of 4. The initial learning rate is $5e-4$ and multiplied by 0.6 every epoch.

For both datasets, we generate a random transformation, which involves a rotation around the up-axis and a translation on the ground within a range of 10 m, to rotate and translate the point cloud. The ground-truth camera poses are

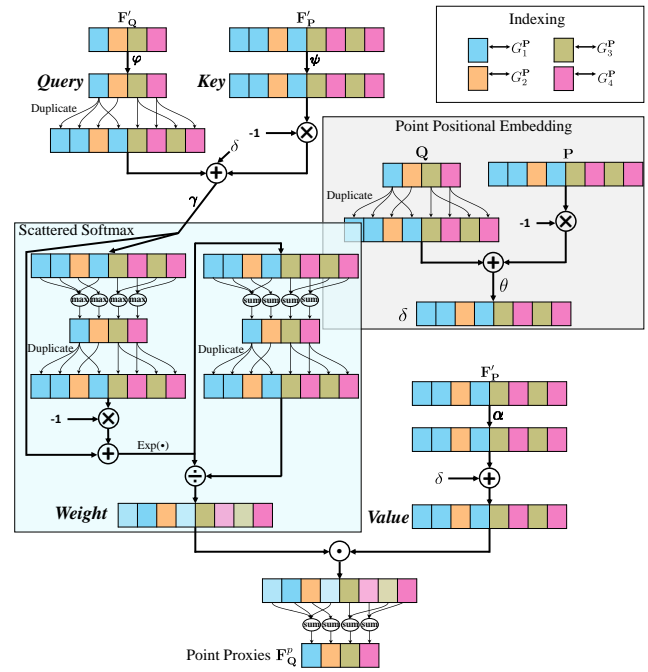


Figure 6: The computation graph of Attentive Aggregation. Different colors index the different point sets.

Input	Image	Point Cloud
Proxy Generation	$160 \times 512 \times 3$	40960×3
	$80 \times 256 \times 64$	1280×64
	$40 \times 128 \times 64$	256×64
Proxy Learning	$5 \times 16 \times 64$	$\Leftrightarrow 256 \times 64$
Nearest Upsampling	$40 \times 128 \times 64$	1280×64
	$40 \times 128 \times 64$	40960×64
...

Table 3: The data flow from input to nearest upsampling on the KITTI Odometry dataset. Symbol \Leftrightarrow represents the cross-attention to exchange cross-modal information.

calculated with the inverse transformation. In the training and testing phases, the reference for the coarse-to-fine sampling is different. Specifically, we refer to the ground truth coarse score matrix to sample pixels and points for training while refer to the predicted coarse score matrix instead for testing.

A.3 Data Flow

We use the proposed framework CFI2P to build point-to-pixel correspondences for a point cloud and image pair. However, considering that the pixel resolution and density of an image are much higher than the point resolution and density of a point cloud, we will downsample the image as $1/4$ of the original dimension during forward propagation and then perform the registration task at the downsampled dimension. Inspired by PointNet++ (Qi et al. 2017b), we implemented the point cloud branch of CFI2P with a 2-level hierarchical architecture to enhance the learning performance.

It means that we use FPS to downsample the point cloud twice while grouping the points and features twice. Thus, the actual feature extraction structure is more complex than the diagram in the Proxy Generation module in Fig. 2.

We show the data flow from input to nearest upsampling on KITTI Odometry in Tab. 3. During proxy generation, we reduce the image resolution twice using ResNet and downsample the point cloud twice using FPS, grouping strategy and attentive aggregation. The 256 point features generated here are directly used as point proxies. The image feature with a resolution of $40 \times 128 \times 64$ will be further divided into patches (with a resolution of 8×8) and linearly projected as the pixel proxies (with a resolution of $5 \times 16 \times 64$). After coarse matching, we will upsample the low resolution proxies to higher resolution for further refining. The image resolution is only restored to $40 \times 128 \times 64$ while the point resolution is first restored to 1280×64 and then 40960×64 . With this 2-level hierarchical structure, in addition to the cross-attention in the proxy learning module, we also perform the cross-attention operation between the first upsampled point features (with a resolution of 1280×64) and image features (with a resolution of $40 \times 128 \times 64$).

A.4 Matching Details

We run the Sinkhorn Algorithm (Sinkhorn and Knopp 1967; Sarlin et al. 2020) in the Optimal Transport module, where the number of iterations is set to 100.

As for the coarse matching, we first remove the slack entries from the raw output matrix of the Optimal Transport module. Supervised by the loss in Eq. 14, smaller matrix values represent weaker correlation between the corresponding point and pixel proxies. Thus, the values smaller than a threshold $\tau_c = 0.01$ will be zeroed to get the final score matrix \mathbf{S} . This operation helps us eliminate a large number of point sets outside the camera’s FoV.

As for the fine matching, we also remove the slack entries from the raw output matrix of the Optimal Transport module. After that, we normalized each column of the matrix to a 1D probability distribution, where each value is the probability that a point can be projected to the corresponding pixel. Note that we also remove the invalid points and pixels according to the sampling masks.

A.5 Coarse-to-fine Sampling Details

To facilitate batch processing for further refining, we have to sample a uniform number (i.e., $n = 65$) of points for each point proxy. However, since point clouds are irregular, some point sets can not satisfy this sampling requirement. For j -th point set, if $|G_j^P| < n$, we will repeatedly sample the points in G_j^P until n points are sampled, although it increases the weights of the repeated points during registration. Random sampling or fixed-point sampling can also be used to replace the above repeated sampling, but we find random sampling will induce a large number of invalid points while fixed-point sampling will make the registration process dominated by the fixed point. To eliminate the negative effects of the above sampling methods, we introduce a binary point mask $M_j^P \in \mathbb{R}^{n \times 1}$, where the first $|G_j^P|$ items are

1 and the last $(n - |G_j^P|)$ items are 0 if $|G_j^P| < n$. With this mask, we can remove the invalid points during the further refining.

Pixel sampling follows a similar principle while is simpler to operate due to the regular structure of the image. For the j -th point proxy, higher \mathbf{S}_{ij} represent stronger correlation between the i -th pixel proxy (i.e., a pixel patch with a resolution of $w \times w$ and $w = 8$). So we sample the pixel proxies of the top $k = 3$ items in the j -th column of \mathbf{S} . We also introduce a similar binary pixel mask $M_j^I \in \mathbb{R}^{m \times 1}$ (i.e., $m = 3 \times 64 = 192$) where the first $k' \times 64$ items are 1 and the last $(3 - k') \times 64$ items are 0 if there are only k' items > 0 in the j -th column of \mathbf{S} and $k' < k$.

B Evaluation Metrics

B.1 Inlier Ratio

Inlier Ratio (IR) is the fraction of inliers among all putative point-to-pixel correspondences. A correspondence is considered as an inlier if the distance between the projected point and the ground-truth pixel is smaller than a threshold τ_d . Denote the estimated correspondence set as \tilde{C} , IR is formulated as:

$$\text{IR} = \frac{1}{|\tilde{C}|} \sum_{(\mathbf{u}_i, \mathbf{p}_i) \in \tilde{C}} \llbracket \|\mathbf{u}_i - \mathcal{F}_p(\mathbf{K}\bar{\mathbf{T}}\mathbf{p}_i)\| < \tau_d \rrbracket, \quad (18)$$

where $\llbracket \cdot \rrbracket$ is the Iverson bracket. Similarly, the *Inlier Ratio* after RANSAC iteration (IRR) is calculated on the set of the retained correspondences after RANSAC iteration.

B.2 Feature Matching Recall

Feature Matching Recall (FMR) is the fraction of data pairs whose inlier ratio is above a threshold τ_m . FMR measures the potential success rate during image-to-point cloud registration, which is formulated as:

$$\text{FMR} = \frac{1}{M} \sum_{i=1}^M \llbracket \text{IR}_i > \tau_m \rrbracket, \quad (19)$$

where M is the number of data pairs in the test dataset and IR_i is the *Inlier Ratio* of the i -th data pair. Similarly, the *Feature Matching Recall* after RANSAC iteration (FMRR) is calculated with the IRR of each data pair.

B.3 Relative Rotation Error

Relative Rotation Error (RRE) measures the differences in rotation angles between the predicted (i.e., $\mathbf{T} = [\mathbf{R}|\mathbf{t}]$) and the ground-truth camera pose (i.e., $\bar{\mathbf{T}} = [\bar{\mathbf{R}}|\bar{\mathbf{t}}]$). We first calculate the relative rotation matrix $\ddot{\mathbf{R}}$ between \mathbf{R} and $\bar{\mathbf{R}}$ as:

$$\ddot{\mathbf{R}} = \mathbf{R}^{-1} \bar{\mathbf{R}}. \quad (20)$$

Then, we convert $\ddot{\mathbf{R}}$ into three Euler angles with respect to the different coordinate axes, and RRE is the sum of these three angles.

B.4 Relative Translation Error

Relative Translation Error (RTE) measures the differences in translation vectors between the predicted and the ground-truth camera pose as:

$$\text{RTE} = \|\mathbf{t} - \bar{\mathbf{t}}\|. \quad (21)$$

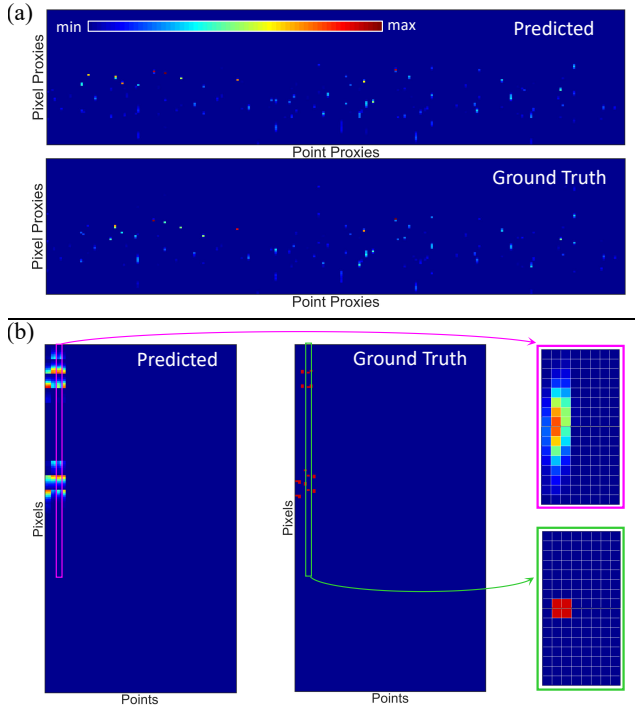


Figure 7: Visualization of the coarse and fine matching score matrices. (a) Coarse matching. (b) Fine matching.

B.5 Registration Recall

Registration Recall (RR) is the fraction of successful registrations in the test dataset. A registration is considered as successful when the RRE is smaller than τ_r and the RTE is smaller than τ_t . So, RR is formulated as:

$$\text{RR} = \frac{1}{M} \sum_{i=1}^M \llbracket \text{RRE}_i < \tau_r \wedge \text{RTE}_i < \tau_t \rrbracket, \quad (22)$$

where RRE_i and RTE_i the relative rotation and translation error of the i -th data pair, respectively.

Following the common practice (Qin et al. 2022; Ren et al. 2022), we only report the RRE and RTE of the successful registrations in Tab. 1. As for the registration recall, the RR values in Tab. 1 fully satisfy Eq. 22 while the RR curves in Fig. 4 (bottom two) only meet one of the conditions of RTE or RRE.

C Additional Results

C.1 Matching Score Matrix

We visualize a real example in Fig. 7. During coarse matching, the ground truth matching score matrix is calculated according to Eq. 13. The vertical axis represents 80 pixel proxies while the horizontal axis represents 256 point proxies. Note that the values of our predicted matching score matrix \mathbf{S} are not exactly correct, but the positions of most scores greater than 0 are accurate. It is enough to provide a reference for the next coarse-to-fine sampling. During fine

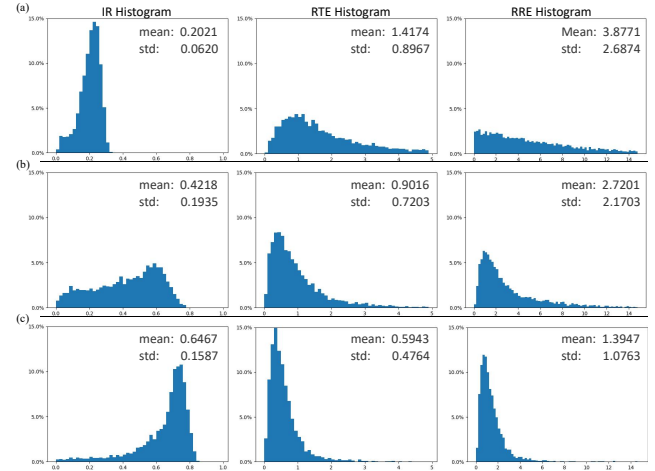


Figure 8: Histograms of IR, RTE and RRE on the KITTI Odometry dataset. x-axis is RTE(m) and RRE($^{\circ}$), and y-axis is the percentage. (a) DeepI2P. IR histogram is obtained with DeepI2P-A. RTE and RRE histograms are obtained with DeepI2P-C. (b) CorrI2P. (c) CFI2P.

matching, the ground truth matching score matrix is calculated according to Eq. 15 and Eq. 16. The vertical axis represents 192 pixels (i.e., the top 3 pixel proxies) while the horizontal axis represents 65 points. Fig. 7 (b) shows a typical example that consists of 128 valid pixels and 7 valid points, since there are only 7 points in the point proxy and only 2 items (i.e., 2 pixel proxies) greater than 0 in the corresponding column of \mathbf{S} . Thus, the right and bottom values are zeroed by the sampling mask in both the predicted and ground truth matching score matrices. We also restore a column of our predicted matching score matrix as 2 pixel patches and concatenate them. As illustrated in the result, each column in the fine matching score matrix can be reshaped as a 2D probability distribution that each 3D point maps onto the image.

C.2 Inlier Ratio and Registration Error Distribution

We visualize the distributions of IR and registration errors (i.e., RTE and RRE) in Fig. 8, where the data are acquired on KITTI Odometry. In addition to higher IR and lower errors, it is evident that CFI2P consistently generates distributions with a smaller width and a higher peak compared to the other two competitors.

C.3 More Correspondence and Registration Results Visualization

To provide a visual proof for the data in Tab. 1, we visualize more point-to-pixel correspondences and image-to-point cloud registration results in Fig. 9. Since the testing dataset is a continuous sequence of camera and LiDAR data, we also provide a dynamic point-to-pixel correspondences video in the multimedia materials.

Point Number	IR(%)	RTE(m)	RRE(°)
5120	32.82	1.175	2.524
10240	39.10	1.061	2.325
20480	57.60	0.670	1.625
40960	64.67	0.594	1.395

Table 4: Ablation studies of the point cloud density.

Point(n)	Pixel(m)	IR(%)	RTE(m)	RRE(°)
65	$1 \times 8 \times 8$	52.02	0.777	1.626
65	$2 \times 8 \times 8$	60.54	0.652	1.467
65	$3 \times 8 \times 8$	64.67	0.594	1.395
65	$4 \times 8 \times 8$	66.09	0.589	1.391
65	$5 \times 8 \times 8$	66.61	0.581	1.371
25	$3 \times 8 \times 8$	68.43	0.661	1.419
35	$3 \times 8 \times 8$	67.49	0.636	1.427
45	$3 \times 8 \times 8$	66.59	0.628	1.416
55	$3 \times 8 \times 8$	65.74	0.606	1.407
75	$3 \times 8 \times 8$	64.01	0.591	1.385
85	$3 \times 8 \times 8$	63.12	0.579	1.389

Table 5: Ablation studies of the coarse-to-fine sampling density.

D Additional Ablation Studies

D.1 Point Cloud Density

We have conducted ablation studies on the KITTI Odometry dataset to further analyze the effect of the point cloud density. As illustrated in Tab. 4, as the number of 3D points decreases, the inlier ratio of the point-to-pixel correspondences also decreases. This is primarily due to the fact that low-density point clouds result in sparse geometric information, which makes it more challenging to extract precise correspondences. Consequently, the accuracy of the registration is also adversely impacted.

D.2 Coarse-to-fine Sampling Density

We have investigated the effect of coarse-to-fine sampling density on KITTI Odometry. For the top 5 rows in Tab. 5, we sample 65 points in each point proxy, while sampling different numbers of pixel proxies (i.e., pixel patches with a resolution of 8×8) separately. It can be seen that when the number of pixels increases, there is an improvement in the performance of CFIP. However, this enhancement gradually diminishes in the later stage. For the bottom 6 rows in Tab. 5, we sample different numbers of points in each point proxy, while the number of pixel proxies is kept at 3. It can be seen that sampling more points makes the IR drop slightly. This is because some sampled points will not fall within the top 3 pixel proxies with high coarse matching scores, so that the correct point-to-pixel correspondences cannot be established. Nevertheless, the registration errors (i.e., RTE and RRE) still show a downward trend as the number of points increases. Despite the slight decrease in IR, there has been an actual increase in the total number of accurate correspondences, which contribute to these improvements.

References

Ao, S.; Hu, Q.; Wang, H.; Xu, K.; and Guo, Y. 2023. BUFFER: Balancing Accuracy, Efficiency, and Generalizability in Point Cloud Registration. In *Proceedings of the IEEE/CVF Conference on Computer Vision and Pattern Recognition*, 1255–1264.

Aoki, Y.; Goforth, H.; Srivatsan, R. A.; and Lucey, S. 2019. Pointnetlk: Robust & efficient point cloud registration using pointnet. In *Proceedings of the IEEE/CVF conference on computer vision and pattern recognition*, 7163–7172.

Besl, P.; and McKay, N. D. 1992. A method for registration of 3-D shapes. *IEEE Transactions on Pattern Analysis and Machine Intelligence*, 14(2): 239–256.

Caesar, H.; Bankiti, V.; Lang, A. H.; Vora, S.; Liong, V. E.; Xu, Q.; Krishnan, A.; Pan, Y.; Baldan, G.; and Beijbom, O. 2020. nuscenes: A multimodal dataset for autonomous driving. In *Proceedings of the IEEE/CVF conference on computer vision and pattern recognition*, 11621–11631.

Chen, X.; Xue, J.; and Pang, S. 2022. Sparse Semantic Map-Based Monocular Localization in Traffic Scenes Using Learned 2D-3D Point-Line Correspondences. *IEEE Robotics and Automation Letters*, 7(4): 11894–11901.

Cui, H.; Tu, D.; Tang, F.; Xu, P.; Liu, H.; and Shen, S. 2022. Vidsfm: Robust and accurate structure-from-motion for monocular videos. *IEEE Transactions on Image Processing*, 31: 2449–2462.

DeTone, D.; Malisiewicz, T.; and Rabinovich, A. 2018. Superpoint: Self-supervised interest point detection and description. In *Proceedings of the IEEE conference on computer vision and pattern recognition workshops*, 224–236.

Diel, D. D.; DeBitetto, P.; and Teller, S. 2005. Epipolar constraints for vision-aided inertial navigation. In *2005 Seventh IEEE Workshops on Applications of Computer Vision (WACV/MOTION'05)-Volume 1*, volume 2, 221–228. IEEE.

Dosovitskiy, A.; Beyer, L.; Kolesnikov, A.; Weissenborn, D.; Zhai, X.; Unterthiner, T.; Dehghani, M.; Minderer, M.; Heigold, G.; Gelly, S.; et al. 2021. An Image is Worth 16x16 Words: Transformers for Image Recognition at Scale. In *International Conference on Learning Representations*.

Durrant-Whyte, H.; and Bailey, T. 2006. Simultaneous localization and mapping: part I. *IEEE Robotics and Automation Magazine*, 13(2): 99–110.

Feng, M.; Hu, S.; Ang, M. H.; and Lee, G. H. 2019. 2d3d-matchnet: Learning to match keypoints across 2d image and 3d point cloud. In *2019 International Conference on Robotics and Automation (ICRA)*, 4790–4796. IEEE.

Fischler, M. A.; and Bolles, R. C. 1981. Random sample consensus: a paradigm for model fitting with applications to image analysis and automated cartography. *Communications of the ACM*, 24(6): 381–395.

Gao, X. S.; Hou, X. R.; Tang, J.; and Cheng, H. F. 2003. Complete solution classification for the perspective-three-point problem. *IEEE Transactions on Pattern Analysis and Machine Intelligence*, 25(8): 930–943.

Geiger, A.; Lenz, P.; Stiller, C.; and Urtasun, R. 2013. Vision meets robotics: The kitti dataset. *The International Journal of Robotics Research*, 32(11): 1231–1237.

He, K.; Zhang, X.; Ren, S.; and Sun, J. 2016. Deep residual learning for image recognition. In *Proceedings of the IEEE conference on computer vision and pattern recognition*, 770–778.

Hoffer, E.; and Ailon, N. 2015. Deep metric learning using triplet network. In *Similarity-Based Pattern Recognition: Third International Workshop, SIMBAD 2015, Copenhagen, Denmark, October 12–14, 2015. Proceedings* 3, 84–92. Springer.

Huang, S.; Gojcic, Z.; Usvyatsov, M.; Wieser, A.; and Schindler, K. 2021. Predator: Registration of 3d point clouds with low overlap. In *Proceedings of the IEEE/CVF Conference on computer vision and pattern recognition*, 4267–4276.

Lee, A. J.; Song, S.; Lim, H.; Lee, W.; and Myung, H. 2023. (LC)²: LiDAR-Camera Loop Constraints For Cross-Modal Place Recognition. *IEEE Robotics and Automation Letters*.

Lepetit, V.; Moreno-Noguer, F.; and Fua, P. 2009. EPnP: An accurate O(n) solution to the PnP problem. *International journal of computer vision*, 81: 155–166.

Li, J.; Chen, B. M.; and Lee, G. H. 2018. So-net: Self-organizing network for point cloud analysis. In *Proceedings of the IEEE conference on computer vision and pattern recognition*, 9397–9406.

Li, J.; and Lee, G. H. 2021. DeepI2P: Image-to-point cloud registration via deep classification. In *Proceedings of the IEEE/CVF Conference on Computer Vision and Pattern Recognition*, 15960–15969.

Li, X.; Han, K.; Li, S.; and Prisacariu, V. 2020. Dual-resolution correspondence networks. *Advances in Neural Information Processing Systems*, 33: 17346–17357.

Liao, Y.; Li, J.; Kang, S.; Li, Q.; Zhu, G.; Yuan, S.; Dong, Z.; and Yang, B. 2023. SE-Calib: Semantic Edges based LiDAR-Camera Boresight Online Calibration in Urban Scenes. *IEEE Transactions on Geoscience and Remote Sensing*.

Lowe, D. G. 1999. Object recognition from local scale-invariant features. In *Proceedings of the seventh IEEE international conference on computer vision*, volume 2, 1150–1157. IEEE.

Lu, F.; Chen, G.; Liu, Y.; Zhang, L.; Qu, S.; Liu, S.; and Gu, R. 2021. Hregnet: A hierarchical network for large-scale outdoor lidar point cloud registration. In *Proceedings of the IEEE/CVF International Conference on Computer Vision*, 16014–16023.

Ma, J.; Jiang, X.; Fan, A.; Jiang, J.; and Yan, J. 2021. Image matching from handcrafted to deep features: A survey. *International Journal of Computer Vision*, 129: 23–79.

Mok, T. C.; and Chung, A. 2022. Affine medical image registration with coarse-to-fine vision transformer. In *Proceedings of the IEEE/CVF Conference on Computer Vision and Pattern Recognition*, 20835–20844.

Mur-Artal, R.; Montiel, J. M. M.; and Tardos, J. D. 2015. ORB-SLAM: a versatile and accurate monocular SLAM system. *IEEE transactions on robotics*, 31(5): 1147–1163.

Qi, C. R.; Su, H.; Mo, K.; and Guibas, L. J. 2017a. Pointnet: Deep learning on point sets for 3d classification and segmentation. In *Proceedings of the IEEE conference on computer vision and pattern recognition*, 652–660.

Qi, C. R.; Yi, L.; Su, H.; and Guibas, L. J. 2017b. Pointnet++: Deep hierarchical feature learning on point sets in a metric space. *Advances in neural information processing systems*, 30.

Qin, Z.; Yu, H.; Wang, C.; Guo, Y.; Peng, Y.; and Xu, K. 2022. Geometric transformer for fast and robust point cloud registration. In *Proceedings of the IEEE/CVF Conference on Computer Vision and Pattern Recognition*, 11143–11152.

Reddy, B. S.; and Chatterji, B. N. 1996. An FFT-based technique for translation, rotation, and scale-invariant image registration. *IEEE transactions on image processing*, 5(8): 1266–1271.

Ren, S.; Zeng, Y.; Hou, J.; and Chen, X. 2022. CorrI2P: Deep Image-to-Point Cloud Registration via Dense Correspondence. *IEEE Transactions on Circuits and Systems for Video Technology*.

Rublee, E.; Rabaud, V.; Konolige, K.; and Bradski, G. 2011. ORB: An efficient alternative to SIFT or SURF. In *2011 International conference on computer vision*, 2564–2571. IEEE.

Rusinkiewicz, S.; and Levoy, M. 2001. Efficient variants of the ICP algorithm. In *Proceedings Third International Conference on 3-D Digital Imaging and Modeling*, 145–152.

Sarlin, P.-E.; DeTone, D.; Malisiewicz, T.; and Rabinovich, A. 2020. Superglue: Learning feature matching with graph neural networks. In *Proceedings of the IEEE/CVF conference on computer vision and pattern recognition*, 4938–4947.

Sinkhorn, R.; and Knopp, P. 1967. Concerning nonnegative matrices and doubly stochastic matrices. *Pacific Journal of Mathematics*, 21(2): 343–348.

Sun, J.; Shen, Z.; Wang, Y.; Bao, H.; and Zhou, X. 2021a. LoFTR: Detector-free local feature matching with transformers. In *Proceedings of the IEEE/CVF conference on computer vision and pattern recognition*, 8922–8931.

Sun, J.; Shen, Z.; Wang, Y.; Bao, H.; and Zhou, X. 2021b. LoFTR: Detector-Free Local Feature Matching with Transformers. In *Computer Vision and Pattern Recognition*.

Thomas, H.; Qi, C. R.; Deschaud, J.-E.; Marcotegui, B.; Goulette, F.; and Guibas, L. J. 2019. Kpconv: Flexible and deformable convolution for point clouds. In *Proceedings of the IEEE/CVF international conference on computer vision*, 6411–6420.

Tsaregorodtsev, A.; Muller, J.; Strohbeck, J.; Herrmann, M.; Buchholz, M.; and Belagiannis, V. 2022. Extrinsic Camera Calibration with Semantic Segmentation. In *2022 IEEE 25th International Conference on Intelligent Transportation Systems (ITSC)*, 3781–3787. IEEE.

Ullman, S. 1979. The interpretation of structure from motion. *Proceedings of the Royal Society of London. Series B. Biological Sciences*, 203(1153): 405–426.

Vaswani, A.; Shazeer, N.; Parmar, N.; Uszkoreit, J.; Jones, L.; Gomez, A. N.; Kaiser, Ł.; and Polosukhin, I. 2017. Attention is all you need. *Advances in neural information processing systems*, 30.

Wang, Y.; and Solomon, J. M. 2019. Deep closest point: Learning representations for point cloud registration. In *Proceedings of the IEEE/CVF international conference on computer vision*, 3523–3532.

Xu, G.; Cheng, J.; Guo, P.; and Yang, X. 2022. Attention Concatenation Volume for Accurate and Efficient Stereo Matching. In *Proceedings of the IEEE/CVF Conference on Computer Vision and Pattern Recognition (CVPR)*, 12981–12990.

Xu, X.; He, L.; Lu, H.; Gao, L.; and Ji, Y. 2019. Deep adversarial metric learning for cross-modal retrieval. *World Wide Web*, 22: 657–672.

Yang, J.; Li, H.; and Jia, Y. 2013. Go-icp: Solving 3d registration efficiently and globally optimally. In *Proceedings of the IEEE International Conference on Computer Vision*, 1457–1464.

Ye, M.; Shen, J.; Lin, G.; Xiang, T.; Shao, L.; and Hoi, S. C. 2021. Deep learning for person re-identification: A survey and outlook. *IEEE transactions on pattern analysis and machine intelligence*, 44(6): 2872–2893.

Yu, H.; Li, F.; Saleh, M.; Busam, B.; and Ilic, S. 2021a. Cofinet: Reliable coarse-to-fine correspondences for robust pointcloud registration. *Advances in Neural Information Processing Systems*, 34: 23872–23884.

Yu, X.; Rao, Y.; Wang, Z.; Liu, Z.; Lu, J.; and Zhou, J. 2021b. Pointr: Diverse point cloud completion with geometry-aware transformers. In *Proceedings of the IEEE/CVF international conference on computer vision*, 12498–12507.

Zhao, H.; Jiang, L.; Jia, J.; Torr, P. H.; and Koltun, V. 2021. Point transformer. In *Proceedings of the IEEE/CVF international conference on computer vision*, 16259–16268.

Zheng, Y.; Kuang, Y.; Sugimoto, S.; Astrom, K.; and Okutomi, M. 2013. Revisiting the pnp problem: A fast, general and optimal solution. In *Proceedings of the IEEE International Conference on Computer Vision*, 2344–2351.

Zhong, Y. 2009. Intrinsic shape signatures: A shape descriptor for 3D object recognition. In *2009 IEEE 12th international conference on computer vision workshops, ICCV workshops*, 689–696. IEEE.

Zhou, Q.; Sattler, T.; and Leal-Taixe, L. 2021. Patch2pix: Epipolar-guided pixel-level correspondences. In *Proceedings of the IEEE/CVF conference on computer vision and pattern recognition*, 4669–4678.

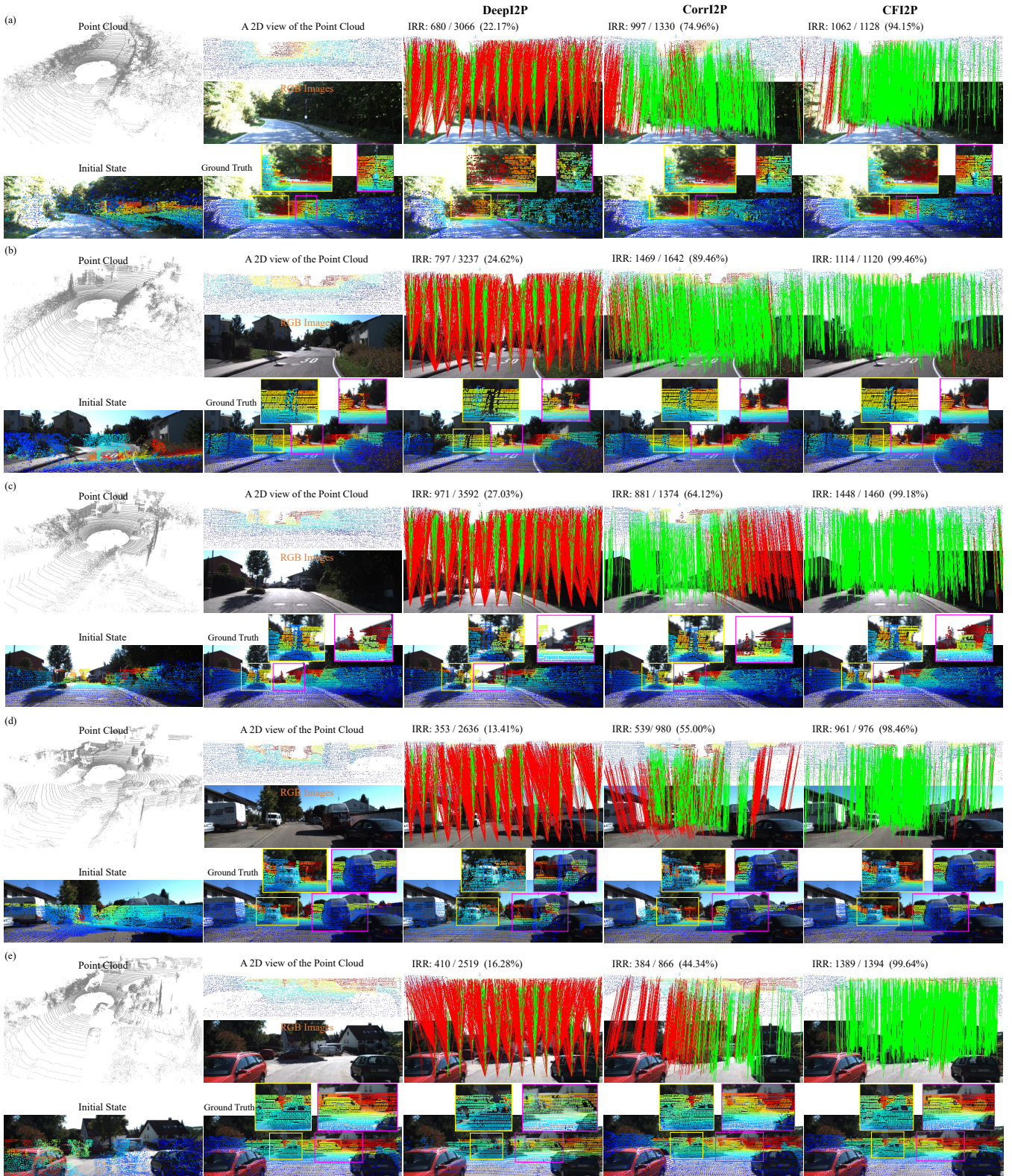


Figure 9: More qualitative results on the KITTI Odometry dataset to supplement Fig.5. Note that many incorrect point-to-pixel correspondences are not within these narrow views, but IRR is calculated from all correspondences.